Lafia Journal of Scientific & Industrial Research (LJSIR), Vol. 4(2), 2026
p-ISSN: 3026 – 9288 e-ISSN: 3027 – 1800 pages: 42–59
https://lafiascijournals.org.ng/index.php/ljsir/index ⇒ Published by the Faculty of Science,
Federal University of Lafia, Nasarawa State, Nigeria

Computational Investigation of 2,3-Dihydroquinazolin-4(1H)-one Derivatives as Multitarget Anti-Alzheimer Agents: DFT and Molecular Docking Studies against AChE, BChE, and BACE1

Abosede Adejoke Badeji[1]*, Olalekan Samuel[2], Segun D. Oladipo[3], Adejoke D. Osinubi[1], Adetoro A. Osanyinbi[1] & Isaac Adebayo Akinbulu[4]

[1]Department of Chemical Sciences, Tai Solarin Federal University of Education, Ijagun, Ogun State, Nigeria
[2]Department of Physiology, Olabisi Onabanjo University, Sagamu Campus, Sagamu, Ogun State, Nigeria
[3]Department of Chemical Sciences, Olabisi Onabanjo University, PMB 2002, Ago-Iwoye, Nigeria
[4]Department of Chemistry, University of Lagos, Akoka-Yaba 101245, Lagos State, Nigeria

Abstract

Alzheimer's disease (AD) remains one of the greatest unmet medical needs worldwide, requiring multitarget therapeutic approach owing to its multifactorial pathogenesis. The 2,3-dihydroquinazolin-4(1H)-one scaffold is a pharmacologically privileged framework with neuroprotective, antioxidant, and enzyme inhibitory activities relevant to AD. Six structurally diverse derivatives (***3a***, ***3k***, ***3m***, ***3n***, ***3r*** and ***3u***) were computationally investigated against three AD-associated targets: acetylcholinesterase (AChE), butyrylcholinesterase (BChE), and β-secretase 1 (BACE1). Molecular electrostatic potential maps, quantum chemical reactivity descriptors and frontier molecular orbital (FMO) analysiswere computed at the M06-2X/def2-TZVP level. Molecular docking was done using Glide/Maestro against co-crystallized protein structure (PDB: 7E3H, 7AIY, 5HU1), with Rivastigmine and Verubecestat as references; cognate-ligand redocking confirmed grid validity.FMO analysis identified ***3n*** as the most reactive within this series (ΔEg = 6.51 eV) and ***3r*** as the most electrophilic (ω = 2.40 eV); these descriptors characterize intrinsic gas-phase electronic properties and do not directly predict docking rank. Molecular docking revealed that ***3k*** achieved the highest binding affinities across all three targets (AChE: −11.22 kcal/mol; BChE: −8.17 kcal/mol; BACE1: −7.78 kcal/mol), substantially outperforming Rivastigmine (AChE: −6.66 kcal/mol; BChE: −5.21 kcal/mol). The superior performance of ***3k*** is attributed to its near-planar geometry, enabling π–π stacking and π–cation contacts within the AChE gorge. Aromatic π–π stacking and hydrogen bonding dominate AChE binding, hydrophobic interactions govern BChE, and polar interactions predominate at BACE1. These results identify ***3k*** as a promising multitarget lead candidate, warranting further experimental validation.

Keywords: Alzheimer's disease, 2,3-Dihydroquinazolin-4(1H)-one, Molecular docking, Density functional theory, Multitarget inhibitors

Article History

Submitted
May 06, 2026

Revised
June 21, 2026

First Published Online
June 29, 2026

Correspondences
A. A. Badeji ✉
ogunlanaaa@tasued.edu.ng

doi.org/10.62050/ljsir2026.v4n2.876

Introduction

Quinazoline and quinazolinone are bicyclic nitrogen containing heterocycles result from fusion of a benzene ring with a pyrimidine ring. These scaffolds correspond to an important family of nitrogen-containing heterocycles with widely ranging and potent biological activity which also exists in several isomeric forms most importantly quinazoline and quinazolinone [1, 2]. The structural flexibility to attach a variety of substituents at several positions has also led to their great pharmacological flexibility in therapeutic areas [3]. Quinazoline derivatives have been of great interest in drug design because of the wide range of their pharmacological activities such as anticancer, anticonvulsant, antibacterial, antifungal, antioxidant, anti-inflammatory, antimalarial and antileukemic activities, especially 4-aminoquinazoline that is found in many drugs and biologically active compounds [2, 4].

Within the structural variants, 2,3-dihydroquinazolin-4(1H)-one is an interesting and particularly privileged molecule with potential for extensive therapeutic applications [1]. Quinazoline derivatives have been shown to have a wide range of therapeutic applications in the treatment of Alzheimer's disease, including modulation and inhibition of amyloid beta, tau protein, cholinesterases, monoamine oxidases and phosphodiesterases and other neuroprotective actions [5]. In more recent times, quinazoline derivatives showed significant antioxidant activity as well as cholinesterase inhibitory and $A\beta_{1-42}$ inhibitory activity making them possible multifunctional drugs for the treatment of Alzheimer's disease [2].

Alzheimer's disease (AD) is the most common neurodegenerative disorder and the leading cause of dementia globally, accounting for approximately 60–80 % of all dementia cases among older adults [6]. The disease is characterized by progressive cognitive decline, memory impairment, language dysfunction, and behavioral disturbances that ultimately interfere with daily functioning and quality of life. With the rapid growth of aging populations worldwide, the prevalence of AD continues to rise substantially, creating a major socioeconomic and healthcare burden. Recent population-based investigations have demonstrated that Alzheimer's disease neuropathological changes (ADNCs) increase significantly with age, affecting more than 65% of individuals older than 90 years, and highlighting the urgent need for improved preventive and therapeutic strategies against this devastating disorder [7]. The pathophysiology of AD is highly complex and multifactorial, involving several interconnected molecular mechanisms. Among the principal pathological hallmarks are extracellular amyloid-beta (Aβ) plaque accumulation, intracellular neurofibrillary tangles composed of hyperphosphorylated tau protein, oxidative stress, mitochondrial dysfunction, synaptic degeneration, and neuroinflammation [8]. The amyloid cascade hypothesis proposes that abnormal accumulation of Aβ peptides initiates neuronal toxicity and triggers downstream neurodegenerative events, whereas the tau hypothesis attributes neuronal dysfunction to abnormal tau phosphorylation and aggregation. In addition, the blood–brain barrier hypothesis suggests that disruption of blood–brain barrier integrity contributes to neuroinflammation and neuronal damage in AD progression [6]. Because of the multifaceted nature of AD pathology, therapeutic agents targeting a single pathway have shown limited clinical success, thereby encouraging the development of multitarget therapeutic strategies.

One of the most extensively studied therapeutic approaches in AD management is the cholinergic hypothesis, which attributes cognitive decline to reduced levels of the neurotransmitter acetylcholine within the brain. Acetylcholine plays a critical role in learning, memory formation, and neuronal communication. In AD patients, degeneration of cholinergic neurons leads to decreased neurotransmitter availability and impaired cognitive function [6]. Acetylcholinesterase (AChE) and butyrylcholinesterase (BChE) are enzymes responsible for the hydrolysis of acetylcholine in the synaptic cleft. Consequently, inhibition of these enzymes has become a major therapeutic strategy for symptomatic treatment of AD [9]. Existing cholinesterase inhibitors such as donepezil, rivastigmine, and galantamine improve cognitive performance temporarily; however, their effectiveness remains limited and they are often associated with adverse side effects. In the search for more potent alternatives, novel quinazoline derivatives [10] designed using the pharmacophoric features of donepezil have demonstrated outstanding AChE inhibitory potential, with the most active compound displaying an IC_{50} value of 9.26 nM against AChE, surpassing that of donepezil itself (IC_{50} = 16.43 nM).

In addition to cholinesterase enzymes, β-secretase (BACE1) has emerged as another important therapeutic target in AD drug discovery. BACE1 catalyzes the initial and rate-limiting step in the cleavage of amyloid precursor protein (APP), leading to the production of neurotoxic Aβ peptides that aggregate into amyloid plaques [11]. Inhibition of BACE1 therefore offers a promising disease-modifying approach aimed at reducing amyloid burden and slowing AD progression. Despite substantial efforts toward the development of BACE1 inhibitors, many clinical candidates have failed because of toxicity concerns, poor blood–brain barrier permeability, or insufficient selectivity.

Current research trends emphasize the design of multitarget-directed ligands capable of simultaneously modulating cholinesterase activity, BACE1 inhibition, oxidative stress, and neuroinflammation to achieve more effective therapeutic outcomes [5, 8, 12]. Several recent investigations have highlighted the therapeutic potential of quinazoline derivatives against AD-associated molecular targets. For instance, quinazoline derivatives designed via lead optimization have been reported to demonstrate dual inhibitory activity against human cholinesterase and BACE1 enzymes, alongside excellent blood–brain barrier permeability and neuroprotective effects in vivo [13]. Similarly, Chandran and co-workers developed quinazolinone-hydrazine cyanoacetamide hybrids with multitarget-directed activity against AChE, oxidative stress, and Aβ aggregation [14]. Their findings revealed strong binding interactions with catalytic and peripheral active sites of AChE and significant neuroprotective effects in neuronal cell models. These studies support the growing interest in quinazoline-based compounds as potential multitarget therapeutic agents capable of addressing the complex pathogenesis of AD more effectively than conventional single-target drugs.

Computational chemistry has emerged as an essential arm in the rational design of anti-AD candidates [15, 16]. The use of computational approach has revolutionized the drug discovery process, notably allowing the identification of biomolecular targets of therapeutic interest and the selection and optimization of lead candidates, as well as the prediction of their pharmacokinetic and pharmacodynamic properties [16, 17], with molecular docking playing a pivotal role in this process [17, 18]. In the particular context of AD, molecular docking, virtual screening and molecular dynamics simulations have been assessed in 100 studies over a 20-year period, and the most common target proteins have been AChE, BACE1 and multi-target approaches, highlighting the role of structure-based in silico approaches in early-stage AD drug discovery [15]. In parallel with docking, density functional theory (DFT) calculations give electronic level information about candidate molecules [19, 20]. In addition to molecular docking, DFT methods have been used to obtain information on the molecular structure, such as

the molecular electrostatic potential mapping, and global reactivity indices including electronegativity, electrophilicity, chemical hardness and softness [19 – 21], leading to the establishment of robust structure–activity correlations for cholinesterase inhibitors [20 – 22]. Combination of DFT and molecular docking with additional support from toxicity profiles of the compoundsis thus a well-validated and efficient computational framework for prioritization of novel anti-AD scaffolds.

In the present study, selected 2,3-dihydroquinazolin-4(1H)-one derivatives, ***3a–3u***, synthesized by the group of Chandrashekharapp, through an aqueous ammonia-mediated green synthetic approach, were investigated for their potential activity against major AD-related targets using in-silico techniques [23]. The compounds were selected because of the pharmacological relevance of the quinazolinone scaffold and the structural diversity introduced through various electron-donating and electron-withdrawing substituents (Scheme 1). Molecular docking studies were employed to evaluate the binding interactions of the compounds with cholinesterase enzymes and BACE1, while DFT calculations were used to examine their electronic properties and chemical reactivity. In addition, the in silico toxicity profiles of the six compounds were conducted using the ProTox 3.0 webserver (https://tox.charite.de) and the pkCSM web server (https://biosig.lab.uq.edu.au/pkcsm), which used molecular similarities and machine-learning models to predict acute oral toxicity, organ toxicities and other toxicological endpoints [24]. The integration of these computational approaches is essential in the identificationof promising quinazolinone-based lead compounds for the development of novel therapeutics against Alzheimer's disease.

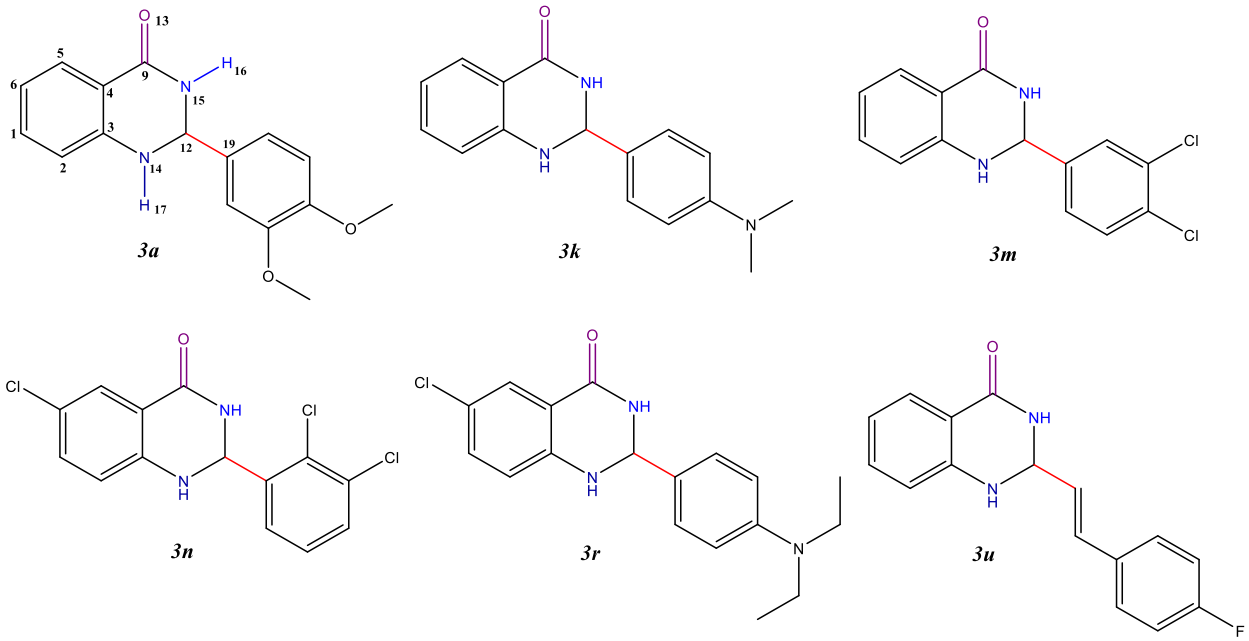

Scheme 1: 2D representation of the compounds examined, with the labelling of selected atoms

Computational Methodology

DFT studies

All density functional theory (DFT) calculations were carried out with the Gaussian 16 software package [25] on the Lengau cluster, located in the Centre for High Performance Computing (CHPC, Cape Town, South Africa; www.chpc.ac.za). All six compounds were fully optimized using the def2-TZVP basis set for all atoms (C, H, N, O, F, and Cl) and M06-2X exchange-correlation functional [26]. The M06-2X functional was selected for this work on the basis of its established performance for thermochemistry, kinetics, and non-covalent interactions in drug-like organic molecules [27]. It has been shown to give reliable molecular geometries and relative reactivity trends across congeneric compound series, making it well-suited for comparative DFT studies of this type [26, 28]. Next, frequency calculations were computed at the same level of theory to ensure that all optimized structures represent true energy minima on the potential energy surface (no imaginary frequencies were found). The pictorial representations of the charge distribution in the molecule, via the molecular electrostatic potential (MESP) map, were obtained to predict the reactivity trends along the series [29 – 31]. The MESP color scheme has been used to show regions of maximum positive, neutral, and maximum negative electrostatic potential, which are electrophilic, neutral, and nucleophilic sites on the molecular surface, respectively. The Frontier molecular orbital (FMO) analysis was used to assess the electronic and reactivity properties of each compound [28, 32, 33]. The highest occupied molecular orbital (HOMO), lowest unoccupied molecular orbital (LUMO) and HOMO–LUMO energy gap (ΔE) were calculated as descriptors

of charge transfer character and chemical reactivity. Within this series, a smaller relative ΔE indicates comparatively greater reactivity and reduced kinetic stability relative to other members of the series [33–35]. The ionization potential (IP = $-E_{HOMO}$) and electron affinity (EA = $-E_{LUMO}$) were calculated from the energies of the HOMO and LUMO. Amore negative HOMO energy (lower HOMO energy) corresponds to a higher IP and a more stable, less electron-donating molecule; a lower energy of the LUMO corresponds to a stronger electron-accepting tendency. The global chemical reactivity descriptors such as the global hardness (η), global softness (σ), the electronegativity (χ) and the electrophilicity index (ω) were calculated from the FMO energies using equations 1–5, where E_L and E_H are the energies of LUMO and HOMO respectively in electron volt (eV);

$$\eta = \frac{IP-EA}{2} \quad (1)$$

$$\sigma = \frac{1}{\eta} \quad (2)$$

$$\mu = \frac{E_H + E_L}{2} \quad (3)$$

$$\chi = -\mu \quad (4)$$

$$\omega = \frac{\mu^2}{2\eta} \quad (5)$$

All optimized geometries and the molecular orbital surfaces were plotted with GaussView 6.0.16 [36] and Chemcraft [37].

Molecular docking procedure

Molecular docking is a computational technique that models the non-covalent binding interactions between ligands and active sites of the protein targets, considering the energy values between functional groups and residues in the active sites of protein [38, 39]. Maestro version 12.8 was used to get chain A of co-crystallized acetylcholinesterase (PDB: 7E3H) [40], butyrylcholinesterase (PDB: 7AIY) [41] and Beta-Secretase 1 (PDB: 5HU1) [42] from the RCSB protein databank. These proteins were preprocessed using the Protein Preparation Wizard with protonation state at pH 7.0 ± 2.0 using Epik [43]. Subsequently, the reference drug for both cholinesterases Rivastigmine (CID: 77991), the reference drug for beta-secretase (CID: 51352361) and our compounds of interest, ***3a***, ***3k***, ***3m***, ***3n***, ***3r*** and ***3u***were prepared in OPLS4 Force Field using the LigPrep wizard of Maestro [44]. Docking was performed using Glide with receptor grid parameters outlined in Table 1 [45].

Table 1: Dimensions of the Grid Box of the proteins docked in this study

Protein Target		X	Y	Z
AChE (7E3H)	Center	-43.62	37.97	-30.28
	Dimensions (Å)	20.00	20.00	20.00
BChE (7AIY)	Center	-20.25	-14.66	41.27
	Dimensions (Å)	20.00	20.00	20.00
BACE 1 (5HU1)	Center	24.56	10.34	22.03
	Dimensions (Å)	20.00	20.00	20.00

Results and Discussion

To determine the safety and drug-likeness profile of all the compounds synthesized by Chandrashekharappa and co-workers [23] in the series of 2,3-dihydroquinazolin-4(1H)-one derivatives, the initial in silico ADMET (Absorption, Distribution, Metabolism, Excretion, and Toxicity) screening was performed before proceeding to the computational investigation. The ProTox 3.0 webserver [24] and the pkCSM webserver [24] were used to evaluate hepatotoxicity, cytotoxicity, blood–brain barrier (BBB) permeability, central nervous system (CNS) permeability, and acute oral toxicity in rats (LD_{50}) in the ADMET evaluation. Of all of the compounds in the product 3 series reported by Chandrashekharappa and co-workers, only six (namely ***3a***, ***3k***, ***3m***, ***3n***, ***3r***, and ***3u***) were found to have acceptable predicted toxicity profiles. They were shown to have favourable permeability across the BBB, CNS and to have predicted therapeutic exposure levels without significant hepatotoxic or cytotoxic liabilities. Hence these six compounds were selected for further computational study such as density functional theory (DFT) quantum chemical analysis and molecular docking analysis with three main target enzyme in Alzheimer's disease: acetylcholinesterase (AChE), butyrylcholinesterase (BChE), and beta-secretase 1 (BACE1).

DFT Studies

Geometry optimization

The geometry optimization of the six dihydroquinazolinone-based molecules, ***3a***, ***3k***, ***3m***, ***3n***, ***3r*** and ***3u***, designed as inhibitors of acetylcholinesterase (AChE) and butyrylcholinesterase (BChE) with a possible application in Alzheimer's disease was carried out at the M06-2X/def2-TZVP level of theory. The optimized geometrical parameters are summarized in Table 2, and the structures are shown in Fig. 1.

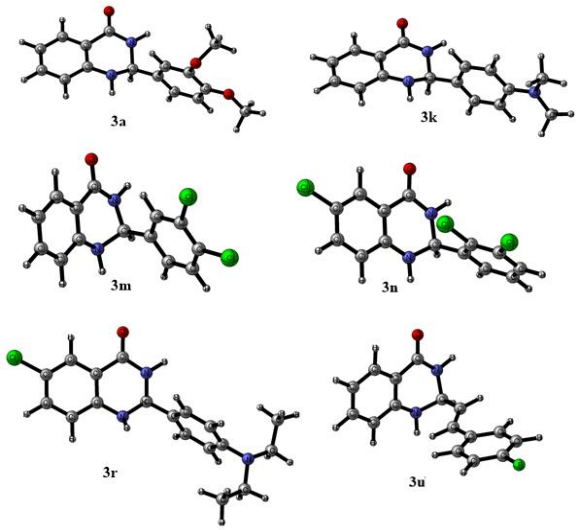

Figure 1 Optimized structures of the six dihydroquinazolinone-based compounds (*3a*, *3k*, *3m*, *3n*, *3r*, and *3u*) computed at the M06-2X/def2-TZVP level of theory

According to Fig. 1, the common core structure of all six compounds is the dihydroquinazolinone bicyclic core, which is composed of a fused benzene ring (Ring A) with a six membered lactam ring (Ring B) containing two nitrogen atoms and a carbonyl group, with an sp^3 methine bridging carbon within ring B connecting the bicyclic core to the pendant aryl group (Ring C). The C=O bond lengths in the lactam were found to be always within a very narrow range of 1.2114–1.2131 Å in the whole series, which indicates high resonance stabilization of the dihydroquinazolinone fragment. The C–N bond length (1.3687–1.3718 Å) is between the single and double bond, confirming the nitrogen lone pair delocalization into the carbonyl, which is typical of lactam systems. The N–H bonds had values of ~1.006–1.010 Å and the C–C–C bond angles in Ring A were essentially ideal (118.7°–121.1°) in all of the structures. It is worth noting that compound ***3n*** shows the shortest N–H value in the series, likely a consequence of the electron-withdrawing effect of the chlorine substituent on ring A, slightly reducing the N–H bond length through inductive effects.

In particular, compound ***3a*** has a dimethoxyl group on ring C.The lactam C=O is 1.2125 Å and C–N15 is 1.3707 Å, which indicates good resonance stability. The C12–C19 linkage between the two aromatic groups (bicyclic ring and ring C) is 1.5056 Å while the dihedral angle (N14–C12–C19–C20) is 124.87° which is to ensure the minimum steric interaction between the two fragments. The C4–C9 aryl–amide bond is 1.4865 Å. Compound ***3k*** is similar to ***3a*** but differ in the ring C (which is a dimethyanilinesystem). The bond lengths of the dihydroquinazolinone in ***3k*** are quite similar with that of ***3a*** (C=O = 1.2131 Å; C9–N15 = 1.3693 Å), suggesting that the dihydroquinazolinone core is insensitive upon substitution of the ring C. The C26–N29 bond of the dimethylaniline is 1.3750 Å, confirming the aromatic delocalization of the aniline ring. The inter-ring dihedral angle is 122.62° which is near to that of ***3a***. In structure, compound ***3m*** in similar to ***3a*** but has the methoxyl groups in ring C of ***3a*** replaced with chlorine atoms in ***3m***. The two bonds C–Cl are each 1.7208 Å and 1.7215 Å respectively, both of which are similar to that of aryl C–Cl bond lengths and are not affected by the bicyclic core C=O (1.2125 Å) and C9–N15 (1.3718 Å) bonds. The most important changes are the increase of the linker bond C12-C19 = 1.5271 Å and a strong decrease in the inter-ring dihedral angle to 78.87°, which is the result of the steric repulsion between the two chlorine atoms forcing the two ring systems to adopt a conformation almost perpendicular to each other.

Table 2: Selected optimized geometric parameters (bond lengths in Å, bond angles and dihedral angles in °) of compounds *3a*, *3k*, *3m*, *3n*, *3r*, and *3u* computed at the M06-2X/def2-TZVP level of theory

Parameter	Description	*3a*	*3k*	*3m*	*3n*	*3r*	*3u*
	Bond Lengths (Å)						
C=O	Lactam carbonyl	1.2125	1.2131	1.2125	1.2119	1.2114	1.2122
C–N (amide)	C–N flanking carbonyl	1.3707	1.3693	1.3718	1.3687	1.3694	1.3717
N14–H17	N–H bond	1.0096	1.0096	1.0097	1.0057	1.0104	1.0083
C4–C9	Aryl–carbonyl bond (Ring A–Ring B)	1.4865	1.4872	1.4824	1.4784	1.4917	1.4845
Linker C12–C19	Bridging Ring B-C	1.5056	1.5031	1.5271	1.5299	1.5078	1.5159
C–N (Ring C)	Aryl C–N (amine) bond	—	1.375	—	—	1.4345	—
	Bond Angles (°)						
C4–C9=O	Carbonyl angle (Ring B)	123.62	123.51	123.82	123.70	123.03	123.68
N14–C12–N15	sp^3 bridge angle (Ring B)	106.93	106.77	107.92	110.16	110.67	107.61
C2–C1–C6	Internal Ring A angle	121.03	121.03	121.06	120.33	119.95	121.02
C3–C4–C5	Internal Ring A angle	120.23	120.24	120.35	120.90	120.60	120.21
	Dihedral Angles (°)						
Inter-ring torsion[c]	Bicyclic core–Ring C orientation	124.87	122.62	78.87	118.44	96.25	~180.00
C4–C9=O13 plane	Amide planarity (Ring B)	~175	~175	~178	~179	~171	~176

The most electronically perturbed compound in the series is ***3n***, with a chlorine atom on Ring A and two on Ring C (same position as ***3m***). The internal angles of the Ring A (118.72°–120.90°) are significantly distorted from ideality and are clearly visible in the chlorine-containing structure, whilst the internal angles in the unsubstituted structures are closer to ideal. The C=O (1.2119 Å) and C9–N14 (1.3687 Å) bonds are the shortest in the series and the C4–C9 bond is the shortest (1.4784 Å), suggesting that there is the greatest degree of amide conjugation due to the electron withdrawing effect of chlorine on Ring A. The linker, C12–C19 bond length is the longest in the series at 1.5299 Å and the inter-ring dihedral angle of 118.44° shows the competing steric effects of the chlorine substituents on both ring A and C. Compound ***3r*** has a chloro substituent on ring A and ring C is diethylaniline, forming the most flexible compound in the series studied. The bond lengths of the C–Cl on ring A (1.7333 Å) is similar to that in ***3n*** and the C=O and C9–N14 bond lengths (1.2114 Å and 1.3694 Å respectively) indicate the same electron-withdrawing effect of chlorine on Ring A. The C24–N29 bond linking Ring C to the diethylaniline nitrogen is 1.4345 Å, as compared to the normal C–N single bond, which shows partial amine–ring delocalization.

The electron donating effect of the dimethylamine group on Ring C outweighs the effect of the chloro substituent, so that the C11–C18 bond (1.5078 Å) is shorter in the present compound than in ***3m*** (1.5271 Å)

and ***3n*** (1.5299 Å). The two fragments are approximately perpendicular to each other because the inter-ring dihedral is 96.25°. The most distinct structure is that of compound ***3u***, which has a linker of type of vinyl C=C bridge, connecting the dihydroquinazolinone fragment with ring C, a fluorobenzene ring, while the other five have a saturated C–C linker. The C–F bond in the ring C is 1.3398 Å, which is typical for a C–F bond with resonance assisting the bond. The core C=O (1.2122 Å) and C9–N14 (1.3717 Å) bond lengths are not particularly noteworthy and indicate that the dihydroquinazolinone core is not significantly affected by the vinyl linkage and fluorine substituent.

This bicyclic structural framework, the dihydroquinazolinone core, is geometrically conserved across all six compounds (C=O range: 0.0017Å; C–N range: 0.0031Å), highlighting the consistent hydrogen bond donor/acceptor pharmacophoric profile regardless of peripheral substitution. The inter-fragment bond (linker) and inter-ring torsion angle are the most structurally variable features, the bond length ranges from 1.5031 (***3k***) to 1.5299 Å (***3n***) and the torsion angle ranges from ~79° (***3m***) to ~180° (***3u***) depending on the steric and electronic effectors of the substituents. The electron withdrawing chlorine on Ring A in ***3n*** and ***3r*** promotes amide conjugation, while the electron donating amino groups and the extended vinyl-fluorobenzene system in ***3k*** and ***3r***, respectively, and promote π – π stacking and hydrophobic interactions in the enzyme active sites. In general, the near-planar geometries of ***3u*** and ***3k*** are more suitable for the elongated gorge of AChE while the bulkier and more twisted geometry of ***3m***, ***3n*** and ***3r*** may be better suited to the wider active site of BChE, as supported by the molecular docking results.

Frontier molecular orbital analysis and Quantum chemical descriptors

The frontier molecular orbital analysis of the investigated compounds (***3a*** to ***3u***) gives useful insights into the electronic properties, stability, and reactivity of the compounds toward the active sites of AChE/BChE/BACE1. From this analysis, quantum chemical descriptors can be obtained as described in the methodology. These descriptors are especially significant in rationalizing the process of ligand-protein interactions in the process of molecular docking.

The energies of the frontier molecular orbital (E_{HOMO} and E_{LUMO}) indicate the electron-donating and electron-accepting capabilities of the compounds (Table 3 and Fig. 2). The E_{HOMO} values ranging between -7.56 to -6.95 eV, represent moderate electron-donating capacity, which is important in interactions with electron-deficient residues in the enzyme binding pocket. Compounds with more negative E_{HOMO} values, like ***3r*** (−7.56 eV) and ***3m*** (−7.50 eV), are less expected to be better electron donors within the series but compounds like ***3k***, with highest E_{HOMO} value (-6.95 eV) is expected to be strongest electron donor and have the greatest potential for hydrogen bonding and charge transfer interactions with amino acid residues in AChE/BChE/BACE1 binding sites. On the other hand, the E_{LUMO} values (−0.64 to -0.16 eV) indicate the electron-accepting ability. Other compounds such as ***3n*** (−0.64 eV) and ***3r*** (−0.61 eV) have the lowest E_{LUMO} energies, indicating the strongest electron-accepting tendency within the series, which may facilitate electron density transfer from nucleophilic residues in the enzyme active sites.

The HOMO-LUMO energy gap (ΔEg), a key measure of chemical reactivity within this series, ranges from 6.51 to 7.16 eV. As noted in the methodology, these values are inflated in magnitude by the high HF exchange fraction of M06-2X, and should not be taken as absolute measures of kinetic stability. Within the series, however, the relative trend is interpretable: compounds with a smaller ΔEg are relatively more reactive and less stable compared with other members of the series, and are more likely to engage in flexible interactions within enzyme binding pockets.

Compound ***3n*** (ΔEg = 6.51 eV) has the lowest energy gap in the series and it is therefore the most reactive compound relative to its congeners, with a comparatively greater tendency toward charge-transfer interactions with the target enzyme active sites. Conversely, compound ***3m*** (ΔEg =7.16 eV) has the widest energy gap in the series and is therefore the most electronically stable and least reactive of the six compounds studied, which may be reflected in its comparatively moderate docking scores.

These trends are further supported by the global reactivity descriptors such as ionization potential (IP), electron affinity (EA), global hardness (η) as well as global softness (σ). The IP values (6.95-7.56 eV) follow the same pattern as E_{HOMO}, which shows the relative ease of donating electrons across the series. The values of the EA (0.16-0.64 eV) confirm that compounds ***3n*** and ***3r*** have the strongest tendency to accept electrons within this group. The global hardness (η), ranging from 3.25 and 3.58 eV, describes resistance to charge transfer, as the lower η corresponds to greater polarizability and reactivity. It is interesting to note that compound ***3n*** has the lowest η value (3.25 eV) and the highest global softness ($\sigma = 0.31\ eV^{-1}$) of the series and is therefore the most reactive compound relative to its congeners, consistent with its narrowest energy gap. Compound ***3m***, with the highest η (3.58 eV), is the most resistant to charge transfer within this series. It should be noted that these rankings describe relative electronic character within the six compounds studied at this level of theory, and do not straightforwardly predict docking rank order, which is additionally governed by steric complementarity and binding-pocket geometry.

The chemical potential (μ) values are negative throughout (−3.56 to −4.09 eV), confirming thermodynamic stability for all compounds, while the corresponding electronegativity values (χ = 3.56–4.09 eV) indicate a general tendency to attract electron density. Among the compounds, ***3r*** has the highest χ value (4.09 eV), suggesting stronger interactions with electron-rich residues in the binding pocket, a property

that may contribute to stabilization via dipole–dipole and hydrogen-bonding interactions relevant to AChE/BChE/BACE1 inhibition.

The electrophilicity index (ω), ranging from 1.86 to 2.40 eV, describes the electrophilic character of each compound. The trend ***3r***>***3n***>***3u***>***3m***>***3a***>***3k*** positions ***3r*** (ω = 2.40 eV) and ***3n*** (ω = 2.33 eV) as the most electrophilic compounds in the series, indicating the strongest tendency to accept electron density from nucleophilic residues in an enzyme active site. Also, compound ***3k*** has the lowest ω value in the series (1.86eV), still it has the highest docking scores across all the three targets that will be discussed subsequently (AChE: -11.2 kcal/mol; BChE: -8.17 kcal/mol; BACE1: -7.78 kcal/mol). These electronic properties are relevant to interactions with nucleophilic residues at the AChE/BChE active-site gorge and the BACE1 aspartyl protease active site. However, it is important to note that global electrophilicity, as a gas-phase property, is one of several factors influencing binding: steric effect, conformational flexibility, and specific non-covalent interaction geometry within the binding pocket also play crucial roles. By itself, it does not govern the binding affinity.

Therefore, compounds ***3n*** and ***3r*** are the most electronically activated members of this series, displaying reduced relative energy gaps, higher global softness, and stronger electrophilicity. These electronic profiles are expected to facilitate charge-transfer and electrostatic interactions with key enzymatic residues. Therefore, these descriptors do not translate to a prediction of the docking rank order. This is because docking affinity demonstrate the integration of electronic, steric, geometric, and solvation factors specific to each binding site. The physical basis for their electronic character and the relationship between these descriptors and the observed protein–ligand interaction profiles are discussed alongside the docking results in Section 3.2.

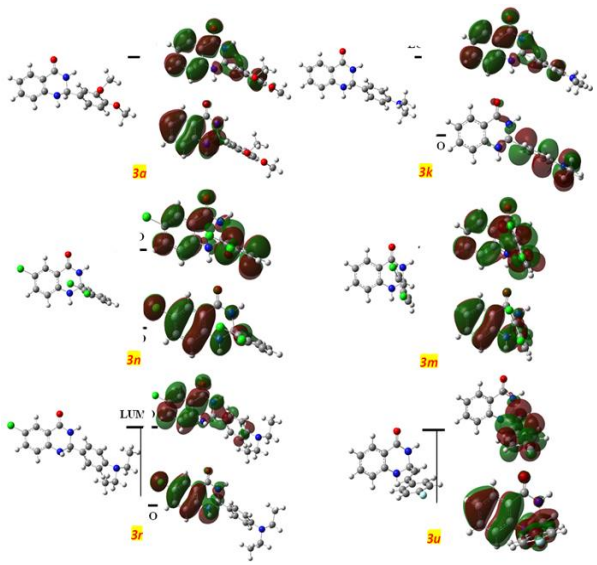

Figure 2: HOMO-LUMO plots of the studied compounds at the M06-2X/def2-TZVPlevel of theory

Table 3: Quantum chemical descriptors of compound *3a*, *3k*, *3m*, *3n*, *3r* and *3u*

Parameters	*3a*	*3k*	*3m*	*3n*	*3r*	*3u*
ELUMO (eV)	-0.26	-0.16	-0.34	-0.64	-0.61	-0.50
EHOMO (eV)	-7.30	-6.95	-7.50	-7.15	-7.56	-7.36
ΔEg (eV)	7.05	6.79	7.16	6.51	6.95	6.86
EA (eV)	0.26	0.16	0.34	0.64	0.61	0.50
IP (eV)	7.30	6.95	7.50	7.15	7.56	7.36
η(eV)	3.52	3.40	3.58	3.25	3.47	3.43
σ (eV^{-1})	0.28	0.29	0.28	0.31	0.29	0.29
μ(eV)	-3.78	-3.56	-3.92	-3.89	-4.09	-3.93
χ (eV)	3.78	3.56	3.92	3.89	4.09	3.93
ω (eV)	2.03	1.86	2.14	2.33	2.40	2.25

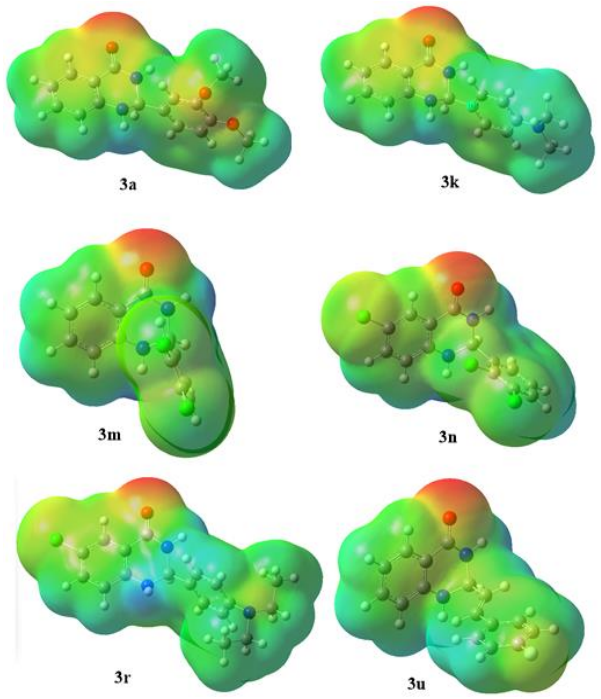

Figure 3: Molecular electrostatic potential map of compound *3a*, *3k*, *3m*, *3n*, *3r* and *3u*

Molecular electrostatic potential analysis

Molecular Electrostatic Potential (MESP) maps of the chosen compounds (***3a–3u***) provide valuable information on the distribution of charges over the molecular surface governing the non-covalent interaction with active sites of AChE/BChE/BACE1. A color scale color ranging between red (region rich in electrons) and blue (region deficient of electrons) was applied to the MESP surfaces with green representing neutral electrostatic potential.

In all compounds, the electron rich areas (red/yellow areas) are largely concentrated around the electronegative atoms like oxygen and nitrogen, especially electronegative atoms in carbonyl, nitro and heterocyclic functionalities. Such areas are likely to become hydrogen bond acceptors and this will enable them to strongly interact with the important amino acid residues within the binding pockets of AChE/BChE/BACE1, including catalytic residues His447 and Ser203 of AChE; His438 and Ser198 of BChE; and the catalytic dyad Asp32 and Asp228 of

BACE1. It is important to note that compounds ***3n*** and ***3r*** have more pronounced negative potential regions, which indicates a greater electron density in the structure, and therefore, a greater potential to form hydrogen bonds and electrostatic interactions (Fig. 3).

Conversely, the electron-deficient regions (blue zones) are predominantly found around hydrogen atoms, and some electron-withdrawing substituents. These regions may serve as hydrogen bond donors and can be involved in an interaction with important electron rich residues such as carbonyl oxygen atoms in the protein backbone. The equal distribution of electron-rich and electron-deficient areas throughout the molecular framework indicates that both donor and acceptor interactions can be involved in these compounds, which is beneficial in maintaining stable ligand binding.

The green region, which represents near-neutral electrostatic potential, dominates the aromatic and hydrophobic parts of the molecules. These areas are probably involved in hydrophobic interactions and π- π stacking with nonpolar residues like Trp86, Phe338, and Tyr337 in the gorge of AChE; Trp82 and Ile442 in BChE; and Phe108, Ile110, and Val69 in the hydrophobic subpockets of BACE1. The extended neutral surfaces suggest that it is well compatible with the hydrophobic parts of the enzyme active sites, which is also a factor in the binding stability in general (Fig. 3).

A comparative study shows that there are slight variations in the electrostatic distribution of the compounds. An example is that ***3m*** has a relatively localized negative potential region, possibly indicating more site-specific interactions, whereas ***3u*** has a more diffused electrostatic surface, potentially enabling broader interactions in the binding cavity. These variations may affect the binding orientation and affinity during docking.

The MESP analysis has been in accordance with the quantum chemical descriptors in the characterisation of the surface electronic properties of the compounds. The compounds ***3n*** and ***3r*** both have the most prominent negative-potential regions around the framework containing the heteroatoms and electron withdrawing substituents well suited to participate in hydrogen bonding and in electrostatic interactions with residues of the AChE/BChE/BACE1 active sites. Compound ***3k***, on the other hand, has a relatively delocalized, neutral-dominated surface throughout the extended aromatic system, consistent with the π–cation and π–π stacking interactions found in docking – interactions, which are driven more by aromatic geometry than by strong electrostatic polarity. These observations show that the MESP surface is not a predictor of binding affinity rank, but rather of the type and mode of interaction.

The overall MESP analysis reveals that each of the six molecules has well-defined regions of both electrophilic and nucleophilic character which are compatible to the active sites examined, and that the differences in electrostatic distribution of the molecules across the series would be expected to affect the binding geometry and mode. The relationship of those electrostatic profiles to the specific binding interactions in molecular docking is discussed in the section below (section 3.2).

Molecular docking

Molecular docking validation

To validate the molecular docking procedure to ensure that the ligands are docked into the search volume of the respective proteins, the docked reference ligands, viz: rivastigmine both cholinesterases, were superimposed on the co-crystalized ligands of the respective proteins as represented in Fig. 4.

To assess the reliability of the docking protocol, the co-crystallized ligand was redocked into the active site. The reproduced pose showed an RMSD value below 1.0 Å relative to the crystallographic conformation, indicating that the docking protocol was capable of satisfactorily reproducing the experimentally observed binding mode and is therefore suitable for subsequent pose prediction studies.

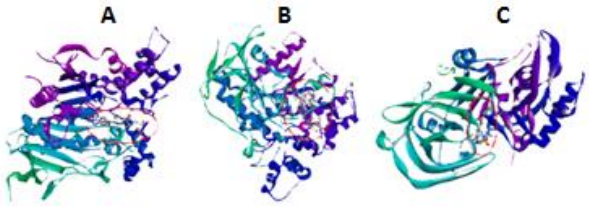

Figure 4: Superimposed ligands in the binding pocket of (A) Acetycholinesterase (B) Butyrylcholinesterase and (C) Beta-Secretase 1

Table 4: Docking scores of reference drugs and selected 2,3-dihydroquinazolin-4(1H)-one derivatives against acetylcholinesterase, butyrylcholinesterase, and β-secretase enzyme

Compound	AChE	BChE	BACE-1)
Rivastigmine (Ref)	-6.66	-5.21	
Verubecestat (Ref)			**-8.91**
3a	-9.14	-6.99	-7.55
3k	-11.22	-8.17	-7.78
3m	-9.04	-7.54	-7.10
3n	-7.47	-7.96	-6.76
3r	-11.14	-7.93	-7.63
3u	-7.69	-7.91	-6.25

Binding affinity

Table 4 presents the molecular docking binding affinity scores of selected 2,3-dihydroquinazolin-4(1H)-one derivatives against three important enzymes associated with Alzheimer's disease, namely acetylcholinesterase (AChE), butyrylcholinesterase (BChE), and β-secretase enzyme (BACE-1). The reference drugs used for comparison were Rivastigmine for AChE and BChE inhibition, and Verubecestat as the reference inhibitor for BACE-1. In molecular docking studies, more negative binding affinity values indicate stronger interactions between the compound and the target enzyme, suggesting better inhibitory potential. The results showed that several of the compounds under

computational investigation demonstrated stronger binding affinities against the target enzymes when compared with the reference compounds.

For acetylcholinesterase (AChE), compound ***3k*** exhibited the strongest binding affinity with a docking score of -11.22 kcal/mol, followed closely by compound ***3r*** with -11.14 kcal/mol. These values were significantly better than the reference drug Rivastigmine, which recorded a docking score of -6.66 kcal/mol, indicating that compounds ***3k*** and ***3r*** may possess stronger inhibitory activity against AChE. Other compounds such as ***3a*** and ***3m*** also demonstrated favorable interactions with AChE, with docking scores of -9.14 kcal/mol and -9.04 kcal/mol respectively, while compounds ***3n*** and ***3u*** showed comparatively weaker interactions.

In the case of butyrylcholinesterase (BChE), compound ***3k*** again recorded the best binding affinity score of -8.17 kcal/mol, followed by compounds ***3n*** (-7.96 kcal/mol), ***3r*** (-7.93 kcal/mol), and ***3u*** (-7.91 kcal/mol). All the compounds under computational investigation demonstrated better binding affinities than Rivastigmine (-5.21 kcal/mol), suggesting promising inhibitory activity toward BChE.

Regarding β-secretase enzyme (BACE-1), the reference inhibitor Verubecestat recorded the strongest binding affinity with a docking score of -8.91 kcal/mol. Among the compounds under computational investigation, compound ***3k*** showed the best interaction with BACE-1, having a docking score of -7.78 kcal/mol, followed closely by compounds ***3r*** (-7.63 kcal/mol) and ***3a*** (-7.55 kcal/mol), therefore only the binding interaction of ***3k*** will be analyzed for BACE-1. Although the compounds under computational investigation did not surpass the binding affinity of Verubecestat, they still exhibited considerable interactions with the BACE-1 enzyme, indicating potential inhibitory activity. Therefore, the findings suggest that compound ***3k*** consistently demonstrated the most promising binding affinities across all three target enzymes, indicating its potential as a multi-target candidate for further investigation in Alzheimer's disease drug development.

It is worth noting that the rank order of the binding affinities listed in Table 4 is not the same as the rank order of the DFT calculated global reactivity descriptors as discussed previously. This difference is not a contradiction, but a reflection of the different quantities that are measured by the DFT descriptors, and by the docking scores, and this is discussed below.

Global reactivity indices such as ΔEg, global softness and the electrophilicity index are properties of isolated molecules that are computed in the gas phase. They describe the ease of a molecule to donate or accept an electron density in a non-directional fashion. Molecular docking scores, on the other hand, are based on the overall free energy of binding within a given protein environment, and incorporate contributions from steric shape complementarity, geometry and directionality of individual non-covalent contacts, desolvation penalties, and precise spatial arrangement of donor and acceptor groups relative to the binding pocket. These are simply site specific quantities that are not intended to be predicted by a global electronic descriptor.

This distinction is clearly demonstrated in compound ***3k***. It has the lowest electrophilicity (ω = 1.86 eV) and mid-range HOMO–LUMO gap (ΔEg = 6.79 eV), and yet it has the highest docking scores for all three targets. The reason can be rationalized based on its molecular geometry. The near-planar orientation of its dimethylaminophenyl ring relative to the dihydroquinazolinone core (inter-ring dihedral 122.62°) produces an extended, flat shape profile that is geometrically complementary to the elongated and aromatic CAS–PAS gorge of AChE. Within this gorge, the dimethylaminophenyl group engages in site-specific π–cation and π–π stacking interactions with TRP86, TYR337, and TYR341, interactions governed by the spatial geometry of aromatic rings rather than by global electrophilicity. These binding-pocket-specific interaction types are not captured by any gas-phase global descriptor. No global gas-phase descriptor is able to account for these types of interactions which occur in the binding pocket.

On the other hand, the compound with the smallest ΔEg (6.51 eV) and the highest softness (σ = 0.31 eV-1) in the series is ***3n,*** with one of the lowest AChE docking scores (−7.47 kcal/mol). It is rationalized that the three-dimensional structure of the molecule: three bulky chlorine substituents are present on ring A and on ring C, and occupy such a highly twisted inter-ring conformation (dihedral ~118°) that gives the molecule a high steric profile. This is a geometry which is not well accommodated by the relatively narrow aromatic gorge of AChE, where steric fit is a major contributing factor of binding affinity. The high softness of the electronic properties of the molecule is not enough to compensate for the poor shape complementarity with the binding site.

This analysis suggests that DFT electronic calculations are complementary to the widely accepted structure-based docking methods in computational medicinal chemistry, where the former describes the intrinsic electronic nature of a compound, while the latter describes the three dimensional fit of the compound with the biological target.

Neither approach alone is enough to describe all the properties of a molecule relevant for drug binding, but when they are combined together, they give a more complete picture of the structure–property landscape of the series. The compound ***3k*** was identified as the most promising candidate because it has consistently better docking scores and it is also favorable in terms of the protein–ligand interaction profile, while compounds ***3n*** and ***3r*** are the most electronically activated compounds, whose electronic properties might be able to support other modes of interaction in different protein environments.

Likewise, ligand protonation states used in docking were generated using Epik at pH 7.0 ± 2.0. Several compounds containing tertiary amine functionalities were predicted to exist partially in protonated forms under physiological conditions. In contrast, DFT

calculations were performed on neutral gas-phase structures. Therefore, the calculated electronic descriptors represent intrinsic properties of the neutral molecules and may not fully reflect the electronic characteristics of the binding-relevant protonated species.

Protein-ligand interaction

To provide a clearer and better understanding of the interactions between favourable 2,3-dihydroquinazolin-4(1H)-one derivatives with the amino acid residues at the protein binding pocket of Acetylcholinesterase, Butyrylcholinesterase and Beta Secretase 1, ligand-protein interaction plots were generated following molecular docking, as shown in Figs 5 – 7 and Tables 5 – 6. From Table 5, the protein–ligand interaction profile of the ligands (***3a***–***3u***) with AChE is dominated by a combination of aromatic π–π stacking, hydrogen bonding, and hydrophobic van der Waals contacts, which is characteristic of the narrow and highly aromatic active-site gorge of AChE.

Key residues such as TRP86, TYR337, TYR341, PHE338, and TRP286 repeatedly appear in π–π and π–alkyl interactions, indicating strong stabilization of ligands through aromatic stacking within both the catalytic active site (CAS) and peripheral anionic site (PAS). Hydrogen bonding interactions, particularly with PHE295, TYR124, ASP74, and HIS447, contribute to ligand orientation and specificity. The presence of π–cation interactions (e.g., TRP86, TYR337) further enhances binding affinity by stabilizing positively charged or polar ligand moieties.

From Table 6, the binding interactions observed for BChE ligands show a stronger emphasis on hydrophobic and alkyl-based interactions, reflecting the larger and more flexible active site of BChE. Residues such as TRP82, PHE329, TRP231, LEU286, and VAL288 frequently participate in π–π, π–alkyl, and van der Waals interactions, indicating that ligand stabilization relies heavily on hydrophobic packing rather than tight aromatic stacking alone. Hydrogen bonding is present but less dominant, mainly involving HIS438 and SER198, which are part of the catalytic machinery. Notably, some ligands also show salt bridge interactions (e.g., with GLU367, ASP70), suggesting stronger or potentially irreversible binding modes in certain cases. The diversity of interaction types including halogen and carbon hydrogen bonds highlights the adaptability of the BChE binding pocket. These interactions suggest that BChE accommodates ligands through broader, less constrained binding driven by hydrophobic complementarity and occasional strong electrostatic or covalent contributions.

Table 5: The binding interactions of Rivastigmine and selected 2,3-dihydroquinazolin-4(1H)-one derivatives in the active site of Acetylcholinesterase

Ligand	Interaction Type	Residues
Rivastigmine	Hydrogen Bond	TYR337, TYR124, TYR341
	Van der Waals	HIS447, PHE297, PHE295, VAL294, SER293, ARG296, TYR72, THR72, TRP439
	π–Cation / Attractive Charge	TRP86, ASP74
	π–π Stacked	PHE338, TYR337, TYR341
	π–Alkyl	TRP286, TYR341
3a	Van der Waals	VAL294, ARG296, PHE297, GLY121, SER125, GLY448, TYR72, ASP74
	Hydrogen Bond	PHE295, HIS447
	π–π (stacked/T-shaped)	TYR124, TRP286, TYR341, PHE338, TYR337
	π–Alkyl	TRP86, TYR337
3k	Van der Waals	VAL294, PHE297, ARG296, GLY448, HIS447, SER203, GLY121, ASP74, TYR72
	Hydrogen Bond	PHE297
	Conventional H-Bond	PHE295
	π–Cation / Attractive Charge	TYR337, TRP86, GLU202
	π–π (stacked/T-shaped)	TYR124, TRP286, TYR341, PHE338
3m	Van der Waals	TYR72, ASP74, GLY121, GLY448, VAL298, ARG296, PHE297
	Conventional H-Bond	PHE295
	π–π (stacked/T-shaped)	TRP286, TYR124, TYR341, TYR337, PHE338
	π–Alkyl	TRP86, HIS447
3n	Van der Waals	THR83, TYR72, GLY448, HIS447, PHE338, PHE297, VAL294, GLY121, GLY122, PHE295
	Conventional H-Bond	ASP74
	π–π (stacked/T-shaped)	TRP86, TYR341, TYR124, TRP286
	π–Alkyl	TYR337
3r	Van der Waals	TYR72, GLY120, GLY121, PHE338, HIS447, VAL294, ASP74, PHE297, GLY448, ARG296
	Conventional H-Bond	TYR124, PHE295
	π–Cation	TRP86
	π–Sigma	TYR341
	π–π Stacked	TRP286, TYR337
3u	Van der Waals	GLY120, GLY121, ASP74, THR83, TYR124, TRP286, SER203, PHE297, GLU202, GLY448, PHE338, VAL294, ARG296
	Conventional H-Bond	SER125, PHE295
	C–H / π-Donor H-Bond	TYR341, TYR337
	π–π Stacked	HIS447, TRP86, TYR341
	π–Alkyl	TYR341, TYR337

Table 6: The binding interactions of Rivastigmine and selected 2,3-dihydroquinazolin-4(1H)-one derivatives in the active site of Butyrylcholinesterase

Ligand	Interaction Type	Residues
Rivastigmine	Carbon H-Bond	GLY115, TYR128, GLU197, SER79
	Conventional H-Bond	TYR332
	Van der Waals	SER198, HIS438, GLY78, GLY439, TRP430, GLY116, TYR440, MET437, PHE329
	Salt Bridge	ASP70
	π–π Stacked	TRP82
	π–Alkyl	ALA328, TRP82
	Van der Waals	PHE398, VAL288, THR120, LEU125, GLY121, VAL127, TRP112, GLY439, PRO285, GLY117
	Conventional H-Bond	HIS438, SER198, TYR128
3a	Carbon H-Bond	GLY115, GLU197, PHE398
	π–π / Amide–π	PHE329, GLY116, TRP231, TRP82, ILE442
	π–Alkyl	LEU286, ILE442, TYR128, TRP82
	Van der Waals	PHE398, SER198, GLY116, ALA328, GLY78, TRP430, SER79, MET437, TYR440, GLY439, PRO285, GLY117, VAL288
	Conventional H-Bond	HIS438
3k	Carbon H-Bond	GLY117, GLY439
	π–Cation	TRP82, HIS438
	π–π T-shaped	TRP231, PHE329
	π–Alkyl	LEU286, TRP231
	Van der Waals	VAL288, GLY117, GLY116, MET437, GLY439, GLU197, SER198, PHE398
3m	Conventional H-Bond	HIS438
	π–π T-shaped	PHE329, TRP231
	π–Alkyl	TYR440, TRP82, ALA328, LEU286, TRP231, PHE329
	Van der Waals	PHE398, SER198, ALA328, GLY439, GLY116, GLY117
	Conventional H-Bond	HIS438
3n	π–π T-shaped	TRP82, TRP231, PHE329, HIS438
	Halogen	LEU286
	Alkyl/π–Alkyl	VAL288, MET437, TYR440
	Van der Waals	GLY439, PHE398, GLY117, THR120, GLY115, GLY116, SER79, TYR332, ASP70, TRP430, GLY78, ALA328, TYR440
	Conventional H-Bond	HIS438
3r	Halogen	LEU286
	π–Cation	TRP82
	π–π T-shaped	TRP231, PHE329
	π–Alkyl	VAL288
	Van der Waals	ALA199, GLY115, THR120, TRP82, HIS438, GLY117, SER79, PHE398, TRP430, LEU286, VAL331, VAL288, PRO285, MET437
	Conventional H-Bond	SER198
3u	Halogen	ALA328
	π-Donor H-Bond	TYR332
	π–π / Amide–π	GLY116, TRP231, PHE329
	π–Alkyl	ALA328

Table 7: The binding interactions of Verubecestat and selected 2,3-dihydroquinazolin-4(1H)-one derivatives (*3k*) in the active site of BACE1

Ligand	Interaction Type	Residues
Verubecestat	Van der Waals	GLN134, GLY95, TYR75, ALA369, GLY74, LEU91, SER96, GLY72, ILE171, TRP176, PHE169, TRP137
	Carbon H-Bond	THR292, SER290, THR293, ASP293
	Halogen	SER71
	Amide–π	GLN73, THR292
	π–Alkyl	TYR132, ILE179
3k	Van der Waals	GLY72, THR293, ILE171, TRP137, PHE169, SER71, LYS70, TYR132, GLY74, TRP176, LEU91, SER290, ILE179, THR292, TYR75, GLN134, GLY135
	Conventional H-Bond	GLY291
	Amide–π	GLN73
	π–Alkyl	ALA396

From Table 7, the interaction pattern for BACE1 differs significantly from cholinesterases, showing a preference for polar, hydrogen bonding, and amide–π interactions rather than extensive aromatic stacking. Residues such as GLY72, GLY74, THR292, SER290, and GLN73 are consistently involved in hydrogen bonding and carbon hydrogen bond interactions, reflecting the importance of stabilizing ligands within the aspartyl protease catalytic environment of BACE1. While some hydrophobic contacts (e.g., with ILE171, LEU91, TYR132) and π–alkyl interactions are present, they play a secondary role compared to polar interactions. The presence of amide–π stacking (GLN73, THR292) further contributes to ligand positioning within the active site. Compared to AChE and BChE, BACE1 binding is more polar and structurally guided, emphasizing precise alignment with catalytic residues rather than deep aromatic enclosure.

This indicates that effective BACE1 inhibitors typically rely on strong hydrogen bonding networks and compatibility with the enzyme's catalytic dyad environment, rather than predominantly hydrophobic or π-driven interactions. Meanwhile, it should be noted that DFT global reactivity descriptors reflect intrinsic electronic properties in isolation, while docking scores reflect complementarity with a specific binding site geometry, steric fit, and specific non-covalent interactions. The dimethylaniline group of ***3k*** provides favourable π–cation and π–π interactions specifically within the AChE gorge that are not captured by global DFT indices alone.

Although all selected compounds were evaluated against BACE1 through molecular docking, detailed interaction analysis was performed only for compound ***3k*** due to its superior docking performance.

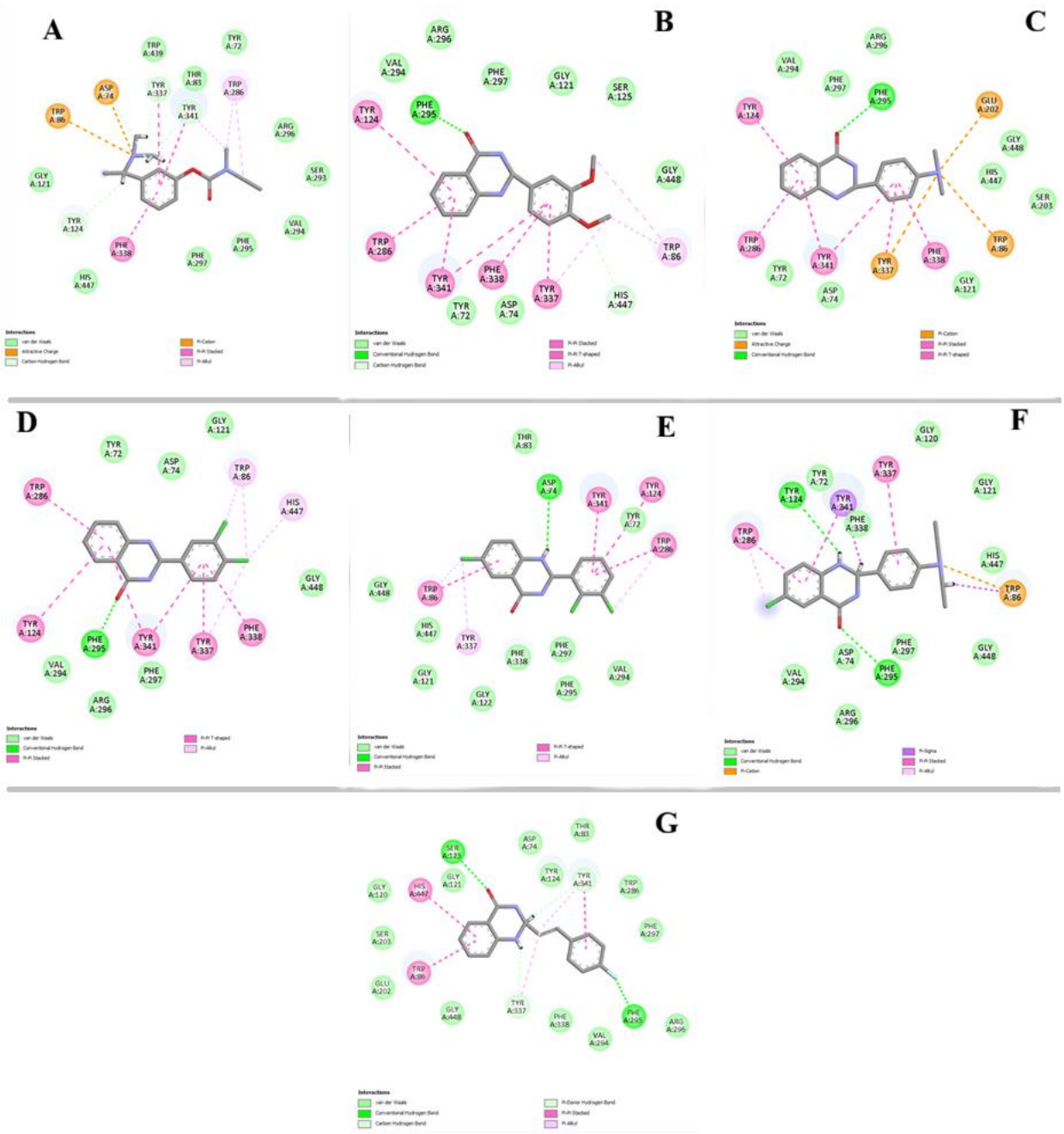

Figure 5: 2D interaction plots of protein-ligand interactions of (A) AChE + Rivastigmine, (B) AChE + *3a*, (C) AChE + *3k*, (D) AChE + *3m*, (E) AChE + *3n*, (F) AChE + *3r*, (G) AChE + *3u*

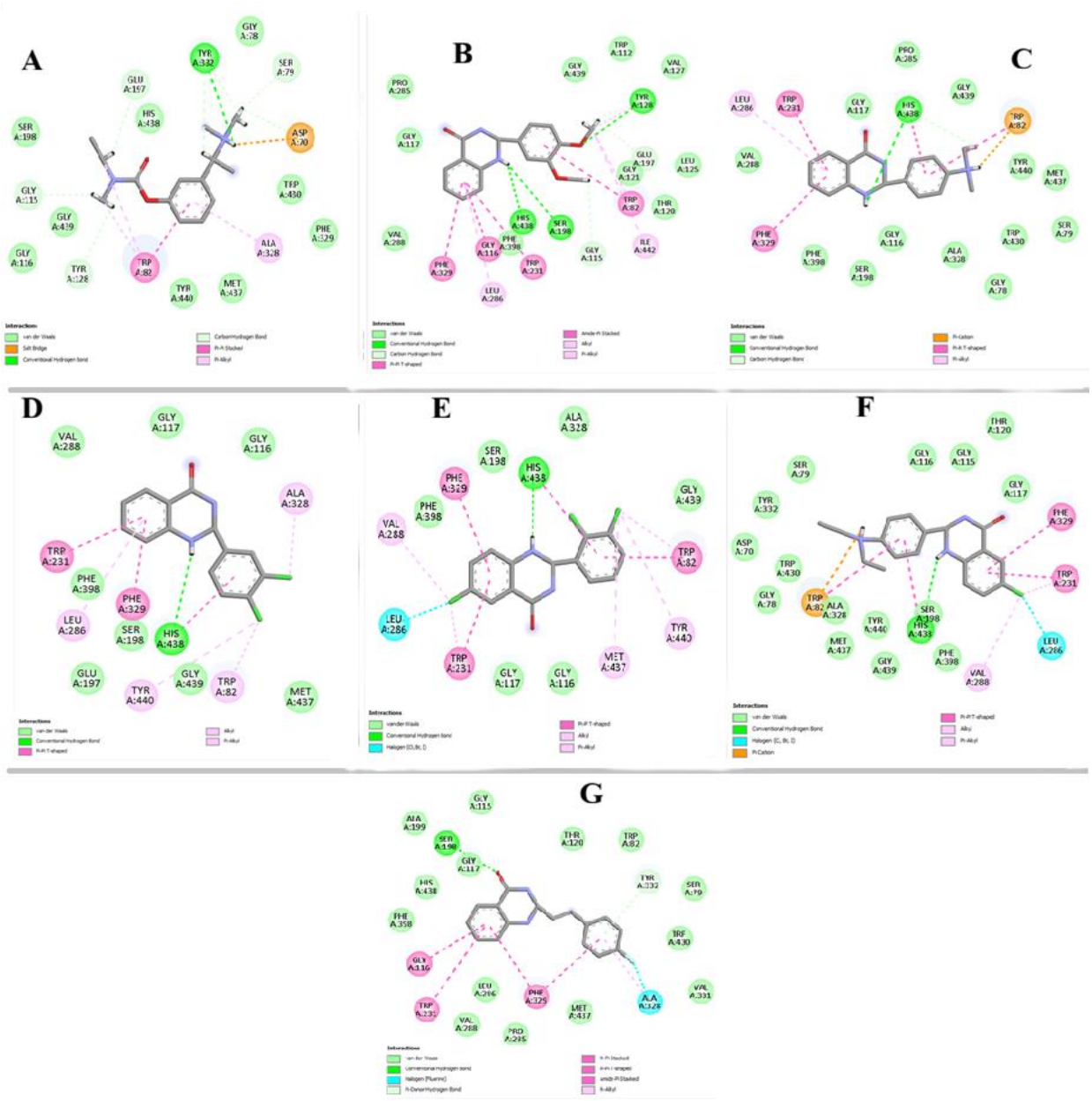

Figure 6: 2D interaction plots of protein-ligand interactions of (A), BChE + Rivastigmine (B) BChE + *3a*, (C) BChE + *3k*, (D) BChE + *3m*, (E) BChE + *3n*, (F) BChE + *3r*, (G) BChE + *3u*

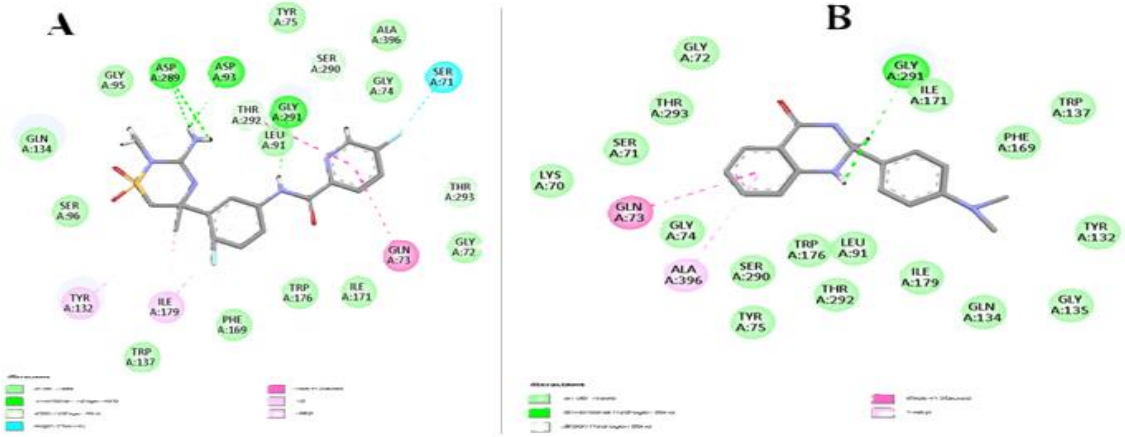

Figure 7: 2D interaction plots of protein-ligand interactions of (A) BACE-1 + Verubecestat, (B) BACE-1 + *3k*

Table 8: Predicted ADMET and drug-likeness properties of synthesized compounds (*3a*, *3k*, *3m*, *3n*, *3r*, and *3u*) in comparison with reference standards rivastigmine and verubecestat

Comp	MW	MF	HBD	HBA	Lipinski Ro5	Human intestinal absorption (% absorbed)	P-glycoprotein substrate	BBB Perm. (log BB)	CNS Perm.	Hepat.	Cytotoxicity	LD_{50} (mol/kg)
3a	284.32	$C_{16}H_{16}N_2O_3$	2	5	Passed	94.6	Yes	0.073	-2.229	Inactive	Inactive	2.382
3k	267.33	$C_{16}H_{17}N_3O$	2	3	Passed	94.0	Yes	0.178	-0.916	Inactive	Inactive	2.492
3m	293.15	$C_{14}H_{10}Cl_2N_2O$	2	2	Passed	90.8	Yes	0.179	-0.884	Inactive	Inactive	2.512
3n	327.60	$C_{14}H_9Cl_3N_2O$	2	2	Passed	88.76	Yes	0.186	-0.937	Inactive	Inactive	2.52
3r	329.83	$C_{18}H_{20}ClN_3O$	2	3	Passed	91.54	Yes	0.125	-1.002	Inactive	Inactive	2.559
3u	268.29	$C_{16}H_{13}FN_2O$	2	2	Passed	92.65	Yes	0.100	-0.958	Inactive	Inactive	2.289
Riv.	250.34	$C_{14}H_{22}N_2O_2$	0	4	Passed	88.46	No	0.508	-2.255	Inactive	Inactive	3.402
Ver.	409.42	$C_{17}H_{17}F_2N_5O_3S$	3	8	Passed	70.90	No	-1.484	-3.121	Inactive	Inactive	1.773

Comp = Compound; Riv. = Rivastigmine; Ver. = Verubecestat; MW = molecular weight; MF = molecular formula; HBD = hydrogen bond donors; HBA = hydrogen bond acceptors; Perm. = permeability; Hepat. = hepatotoxicity; Ro5 = Lipinski's Rule of Five; BBB = blood–brain barrier; CNS = central nervous system; log BB = logarithm of the brain-to-blood concentration ratio; LD_{50} = median lethal dose (mol/kg). Hepatotoxicity and cytotoxicity predictions were obtained from ProTox 3.0; Active = adverse endpoint predicted; Inactive = adverse endpoint not triggered. All six synthesized compounds passed Lipinski's Rule of Five criteria (MW ≤ 500 g/mol, HBD ≤ 5, HBA ≤ 10, LogP ≤ 5). BBB permeability classification: log BB > 0 = penetrant; −1.0 ≤ log BB ≤ 0 = borderline; log BB < −1.0 = non-penetrant. CNS permeability classification: > −2.0 = penetrant; −2.0 to −3.0 = borderline; < −3.0 = non-penetrant.

Pharmacokinetic evaluation, blood-brain barrier permeability, and drug-likeness profiling of the studied compounds

A comparative study of the ADMET and drug-likeness profile of the six potential multi-target-directed ligands for Alzheimer's disease (***3a***, ***3k***, ***3m***, ***3n***, ***3r*** and ***3u***) against the enzyme targets, AChE, BChE, and BACE1, is presented in Table 8. It is essential that these multi-target inhibitors are in silico profiled with reference standards, to confirm that the inhibitors have the required pharmacokinetic properties for activity in the central nervous system. All six compounds meet Lipinski's Rule of Five parameters, which suggest good bioavailability when administered orally. Excellent predicted human intestinal absorption percentages (ranging from 88.76 to 94.60 %) also support this structural drug-likeness. Interestingly, these values are similar to, or greater than, those of the clinical cholinesterase inhibitor Rivastigmine (88.46 %) and significantly higher than that of the reference BACE1 inhibitor Verubecestat (70.90 %). Central compartment delivery is a critical criterion for an effective anti-Alzheimer's ligand as it has to overcome the protective biological barriers to access the intracellular BACE1 and synaptic cholinesterases. Compounds ***3k***, ***3m***, ***3n***, ***3r*** and ***3u*** have very good passive permeability, being highly penetrant in both blood brain barrier (BBB) and CNS permeability models. On the other hand compound ***3a*** is a borderline penetrant for both barriers whereas the reference standard Rivastigmine shows a high overall partition BBB value (0.508) but a lower rate of penetration of the membrane (CNS borderline). Verubecestat is not very active in this passive diffusion model, with both biological barrier activities at the completely non-penetrant range. One of the major pharmacological problems pointed out for the whole synthesized series (***3a***–***3u***) is the fact that they are all substrates of P-glycoprotein. Although active clearance seems to be well balanced for these molecules, based on the active ATP-dependent efflux pump activity of P-glycoprotein at the BBB, active clearance at the BBB may limit brain accumulation of leads such as ***3m*** and ***3n*** that are excellent passive permeability markers, hence warrants further in vivo investigation. Rivastigmine does not undergo this biological barrier since it is not a P-gp substrate. The studied series has an exceptionally clean profile from a safety point of view since all six compounds have been classified as inactive in terms of hepatotoxicity and cytotoxicity with safe median lethal dose (LD_{50}) values ranging from 2.289 to 2.559 mol/kg. This gives compound ***3m***, ***3n***, ***3k***, ***3r*** and ***3u*** a distinct safety advantage over Verubecestat, which has a lower LD_{50} of 1.773 mol/kg, and provides a distinct advantage over the other compounds in this paper in terms of passive barrier permeability, oral absorption, and safety data. Future optimization of this scaffold should aim to make structural changes to avoid P-glycoprotein efflux to maximize the therapeutic inhibition of AChE, BChE, and BACE1 in the brain tissue.

Conclusion

The computational investigation of 2,3-dihydroquinazolin-4(1H)-one derivatives as multitarget anti-Alzheimer agents via density functional theory and molecular docking studies against AChE, BChE, and BACE1 has been carried out in this study. Six 2,3-dihydroquinazolin-4(1H)-one derivatives (***3a***, ***3k***, ***3m***, ***3n***, ***3r*** and ***3u***) have been investigated by means of DFT analysis and molecular docking, and the results obtained are consistent and mechanistically coherent and suggest the versatility of this scaffold as a multitarget anti-Alzheimer agent. Geometry optimization at the M06-2X/def2-TZVP level showed that the dihydroquinazolinone bicyclic core is a spectator in the whole series of molecules, with the C=O bond lengths between 1.2114 and 1.2131 Å, and the C–N bond lengths between 1.3687 and 1.3718 Å, indicating that the lactam pharmacophore is preserved along the whole series irrespective of the peripheral groups. The most structurally variable features, governed by the electronic and steric properties of the substituents, are the inter-ring torsion angle and the length of the linker bond, with the near planar conformation of ***3k*** and ***3u*** being more accommodated by the elongated gorge of AChE, whereas the more

twisted conformers of ***3m***, ***3n***, and ***3r***, appear better suited to the broader active site of BChE.

The frontier molecular orbital (FMO) analysis suggested that the compounds ***3n*** and ***3r*** are the most electronically activated members of the series based on their reduced relative energy gaps, high global softness and strong electrophilicity. The compound ***3n*** has the lowest ΔEg value (6.51 eV), which indicates it as the most chemically reactive within the series, showing the greatest polarizability and tendency toward charge-transfer interactions. Compound ***3m***, however, is the most electronically stable and least reactive of the series with its highest ΔEg (7.16 eV). The global reactivity descriptors support these trends: compound, ***3n*** has the lowest global hardness (η = 3.25 eV) and the highest global softness (σ = 0.31 eV^{-1}), while compound ***3r*** has the highest electrophilicity index (ω = 2.40 eV), indicating the greatest tendency to accept electron density from nucleophilic active-site residues. Together, ***3n*** and ***3r*** are the most electronically activated in this series, having complementary electronic profiles that are applicable to the enzyme environments studied. It is noteworthy, however, that these gas-phase electronic descriptors do not predict the docking rank order of the series: compound ***3k***, the weakest electrophile (ω = 1.86 eV) and with a medium energy gap (ΔEg = 6.79 eV), consistently exhibits the highest binding affinities in all three targets. This result reflects a well-established principle in computational medicinal chemistry: that global DFT reactivity indices and structure-based docking scores reflect complementary, but different, aspects of molecular behaviour. The descriptors calculated by DFT show intrinsic electronic character, whereas the docking scores are based on steric shape fit, binding-pocket geometry, and directionality of specific non-covalent contacts. In the present series, structural and geometric factors, particularly the near-planar conformation of ***3k*** and the specific π–cation and π–π interactions it engages within the AChE gorge, governed the binding hierarchy rather than global electronic reactivity.

These electronic profiles were confirmed by the molecular electrostatic potential (MESP) mapping, which revealed more pronounced electron-rich regions around the carbonyl and heteroatom groups of ***3n*** and ***3r***, well-positioned to promote hydrogen bonding and charge-transfer interactions with key residues across the three binding sites. The molecular docking results revealed that compound ***3k*** is the most promising molecule against all three enzymes, with scores of −11.22 kcal/mol, −8.17 kcal/mol, and −7.78 kcal/mol for AChE, BChE, and BACE1, respectively, which is significantly higher than the reference drug Rivastigmine for the cholinesterase targets (score of −6.66 kcal/mol for AChE and −5.21 kcal/mol for BChE). However, none of the compounds investigated computationally surpassed the binding affinity of the BACE1 reference inhibitor, Verubecestat (−8.91 kcal/mol), and both ***3k*** and ***3r*** showed significant affinity to BACE1, while also displaying excellent affinity to the cholinesterases, indicative of a multipotent profile. The analysis of the protein–ligand interaction profiles identified aromatic π–π stacking and hydrogen bonding in the catalytic and peripheral anionic sites as the most relevant interactions for the binding of AChE, hydrophobic packing as the most relevant interaction for the binding of BChE, and polar interactions and hydrogen bonding in the catalytic dyad environment as the most relevant interactions for the binding of BACE1.

Taking these points into consideration, compound ***3k*** is chosen as the lead compound in this series for further in vitro and in vivo studies, as it has the best docking score for all three targets of the Alzheimer's disease and has a clear interaction profile of π–π stacking, π–cation contacts, and hydrogen bonding. Compound ***3r*** can be considered as a secondary candidate, as it has a good AChE binding affinity (−11.14 kcal/mol) with complementary electronic profile, which may help in the development of a multitarget therapeutic agent. Implementing electron-donating and electron-withdrawing groups on the 2,3-dihydroquinazolin-4(1H)-one scaffold provides significant structure–activity relationships which could be used to design more potent and selective anti-Alzheimer candidates. Nevertheless, it is noteworthy to mention that these findings are merely computational predictions and further experimental evidence on the anti-Alzheimer effect of these compounds based on in vitro and in vivo studies is further required to validate their biological efficacy, safety and therapeutic potential.

Conflict of interest: The authors declare no conflict of any interest.

References

[1] Ghoneim, M. M., Abdelgawad, M. A., Elkanzi, N. A. A., Parambi, D. G. T., Alsalahat, I., Farouk, A. & Bakr, R. B. (2024). A literature review on pharmacological aspects, docking studies, and synthetic approaches of quinazoline and quinazolinone derivatives. *Archiv Der Pharmazie*, 357(8), 2400057. https://doi.org/10.1002/ardp.202400057

[2] Kalakwade, A., Kavalapure, R. S., Gharge, S., Alegaon, S. G., Ranade, S. D., Wong, L. S. & Ramu, R. (2026). Heterocyclic compounds with diverse biological activities: A review of quinazoline and quinazolinone derivatives. *Results in Chemistry*, 19, 102932. https://doi.org/10.1016/j.rechem.2025.102932

[3] Tokalı, F. S. (2025). Recent advances in quinazolinone derivatives: Structure, design and therapeutic potential. *Future Medicinal Chemistry*, 17(9), 1071–1091. https://doi.org/10.1080/17568919.2025.2504327

[4] Haneen, D. S. A., Abdalha, A. A., Alkhatib, M. M., Kamal, M., Youssef, A. S. A., Abou-Elmagd, W. S. I. & Samir, S. S. (2025). Synthesis, comprehensive in silico studies, and cytotoxicity evaluation of novel quinazolinone derivatives as potential anticancer agents. *Scientific Reports*, 15(1), 23697. https://doi.org/10.1038/s41598-025-08062-7

[5] Tokalı, F. S., Taslimi, P., Tuzun, B., Karakuş, A., Sadeghian, N. & Gulçin, İ. (2023). Novel Quinazolinone Derivatives: Potential Synthetic Analogs for the Treatment of Glaucoma, Alzheimer's Disease and Diabetes Mellitus. *Chem. & Biodiversity*, 20(10), e202301134. https://doi.org/10.1002/cbdv.202301134

[6] Liu, J., Yang, B. & Zhang, X. (2024). Theories of Alzheimer's disease: Amyloid hypothesis, blood-brain barrier hypothesis and cholinergic hypothesis. In *E3S Web of Conferences,* 553, 05036. EDP Sciences.

[7] Aarsland, D., Sunde, A. L., Tovar-Rios, D. A., Leuzy, A., Fladby, T., Zetterberg, H., Blennow, K., Tan, K., De Santis, G. & Yakoub, Y. (2026). Prevalence of Alzheimer's disease pathology in the community. *Nature*, 650(8100), 182–186. https://www.nature.com/articles/s41586-025-09841-y

[8] Fronza, M. G., Alves, D., Praticò, D. & Savegnago, L. (2023). The neurobiology and therapeutic potential of multi-targeting β-secretase, glycogen synthase kinase 3β and acetylcholinesterase in Alzheimer's disease. *Ageing Research Reviews*, 90, 102033. https://www.sciencedirect.com/science/article/pii/S1568163723001927

[9] Adeowo, F. Y., Elrashedy, A. A., Ejalonibu, M. A., Lawal, I. A., Lawal, M. M. & Kumalo, H. M. (2022). Pharmacophore mapping of the crucial mediators of acetylcholinesterase and butyrylcholinesterase dual inhibition in Alzheimer's disease. *Molecular Diversity*, 26(5), 2761–2774. https://doi.org/10.1007/s11030-022-10377-w

[10] Al-Karmalawy, A. A., Mohamed, A. F., Shalaby, H. N., Elmaaty, A. A., El-Shiekh, R. A., Zeidan, M. A., Alnajjar, R., Alzahrani, A. Y. A., Al Mughram, M. H., Shaldam, M. A. & Tawfik, H. O. (2025). Donepezil-based rational design of *N* -substituted quinazolinthioacetamide candidates as potential acetylcholine esterase inhibitors for the treatment of Alzheimer's disease: *In vitro* and *in vivo* studies. *RSC Medic. Chem.*, 16(5), 2078–2097. https://doi.org/10.1039/D4MD00778F

[11] Arya, R., Jain, S., Paliwal, S., Madan, K., Sharma, S., Mishra, A., Tiwari, P. & Kadiri, S. K. (2024). BACE1 inhibitors: A promising therapeutic approach for the management of Alzheimer's disease. *Asian Pacific Journal of Tropical Biomedicine*, 14(9), 369–381. https://journals.lww.com/aptb/fulltext/2024/14090/bace1_inhibitors__a_promising_therapeutic_approach.1.aspx

[12] Abualassal, Q., Abudayeh, Z., Sirhan, A. & Mkia, A. (2025). Exploring quinazoline as a scaffold for developing novel therapeutics in Alzheimer's disease. *Molecules*, 30(3), 555.

[13] Verma, A., Waiker, D. K., Singh, N., Roy, A., Singh, N., Saraf, P., Bhardwaj, B., Krishnamurthy, S., Trigun, S. K. & Shrivastava, S. K. (2024). Design, synthesis, and biological investigation of quinazoline derivatives as multitargeting therapeutics in Alzheimer's disease therapy. *ACS Chemical Neuroscience*, 15(4), 745–771. https://doi.org/10.1021/acschemneuro.3c00653

[14] Chandran, R., Dileep, K. V., Gorantla, S. C., Jeelan Basha, S., Mothukuru, S., Siva Kumar, I., Vamsi, K., Kumar, S., Reddy, A. B. M. & Subramanyam, R. (2024). Quinazolinone-hydrazine cyanoacetamide hybrids as potent multitarget-directed druggable therapeutics against Alzheimer's disease: Design, synthesis, and biochemical, in silico, and mechanistic analyses. *ACS Chemical Neuroscience*, 15(18), 3401–3420. https://europepmc.org/article/med/39235838

[15] Azmal, M., Paul, J. K., Shohan, Md. N. H., Haque, A. N. M. S. N. B., Mrinmoy, M., Talukder, O. F. & Ghosh, A. (2025). Evaluating computational and experimental approaches in early-stage Alzheimer's drug discovery: A systematic review. *Journal of Computer-Aided Molecular Design*, 39(1), 27. https://doi.org/10.1007/s10822-025-00610-7

[16] Mihai, D. P. & Nitulescu, G. M. (2025). Computer-aided drug design and drug discovery. *Pharmaceuticals*, 18(3), 436.

[17] Ferreira, L., Dos Santos, R., Oliva, G. & Andricopulo, A. (2015). Molecular docking and structure-based drug design strategies. *Molecules*, 20(7), 13384–13421. https://doi.org/10.3390/molecules200713384

[18] Pinzi, L. & Rastelli, G. (2019). Molecular docking: Shifting paradigms in drug discovery. *Int. J. of Molecular Sci.,* 20(18), 4331.

[19] Gürer, E. S., Kaya, S., Berisha, A. & Morales-Bayuelo, A. (2025). On the effect of conceptual density functional theoretical descriptors in the inhibition of acetylcholinesterase enzyme: Gallic acid derivatives. *Journal of the Indian Chemical Society*, 102(8), 101831.

[20] Hasan, A. H., Abdulrahman, F. A., Obaidullah, A. J., Alotaibi, H. F., Alanazi, M. M., Noamaan, M. A., Murugesan, S., Amran, S. I., Bhat, A. R. & Jamalis, J. (2023). Discovery of novel Coumarin-Schiff base hybrids as potential acetylcholinesterase inhibitors: Design, synthesis, enzyme inhibition, and computational studies. *Pharmace.*, 16(7), 971. https://doi.org/10.3390/ph16070971

[21] Abdullah, N., Hussain, F., Ullah, N., Fatima, H., Tahir, M. A., Rashid, U. & Hassan, A. (2025). Synthesis, pharmacological evaluation, and molecular modeling of phthalimide derivatives as monoamine oxidase and cholinesterase dual inhibitors. *ACS Omega*, 10(10), 10385–10400.

[22] Morales-Bayuelo, A., Baldiris, R. & Vivas-Reyes, R. (2013). Scale alpha and beta of quantitative convergence and chemical reactivity analysis in dual cholinesterase/monoamine oxidase inhibitors for the Alzheimer disease treatment using density functional theory (DFT). *Journal of Theoretical Chemistry*, 2013(1), 768185.

[23] Chandrashekharappa, S., Mogali, N. M., Sagar, T. K., Guliani, G., Barick, S., Behera, B. K., Khan, A. & Tiwari, P. (2025). Aqueous ammonia mediated catalyst-free green synthesis of 2, 3-dihydroquinazolin-4 (1H)-one derivatives. *Tetrahedron*, 134997. https://www.sciencedirect.com/science/article/pii/S0040402025005538

[24] (a) Banerjee, P., Kemmler, E., Dunkel, M., & Preissner, R. (2024). ProTox 3.0: A webserver for the prediction of toxicity of chemicals. *Nucleic Acids Research*, 52(W1), W513–W520; (b) Pires, D. E. V., Blundell, T. L. & Ascher, D. B. (2015). pkCSM: Predicting small-molecule pharmacokinetic and toxicity properties using graph-based signatures. *Journal of Medicinal Chemistry*, 58(9), 4066–4072. https://doi.org/10.1021/acs.jmedchem.5b00104/

[25] Frisch, M., Trucks, G., Schlegel, H., Scuseria, G., Robb, M., Cheeseman, J., Scalmani, G., Barone, V., Petersson, G. & Nakatsuji, H. (2016). Gaussian 16 Revision C. 01, 2016. *Gaussian Inc. Wallingford CT*, 1, 572.

[26] Hohenstein, E. G., Chill, S. T. & Sherrill, C. D. (2008). Assessment of the performance of the M05−2X and M06−2X exchange-correlation functionals for noncovalent interactions in biomolecules. *Journal of Chemical Theory and Computation*, 4(12), 1996–2000.

[27] Zhao, Y. & Truhlar, D. G. (2008). Exploring the limit of accuracy of the global hybrid meta density functional for main-group thermochemistry, kinetics, and noncovalent interactions. *Journal of Chemical Theory and Computation*, 4(11), 1849–1868. https://doi.org/10.1021/ct800246v

[28] Oladipo, S. D., Luckay, R. C., Badeji, A. A., Zamisa, S. Z., Olalekan, S. O. & Oladoye, P. O. (2025). Structural studies, DFT computational analysis and inhibitory potential of (E)-N'-(2-bromophenyl)-N-(2,6-diisopropylphenyl) formamidine against CDK1 and CDK2. *Journal of Molecular Structure*, *1320*, 139734. https://doi.org/10.1016/j.molstruc.2024.139734

[29] Liu, L., Miao, L., Li, L., Li, F., Lu, Y., Shang, Z. & Chen, J. (2018). Molecular electrostatic potential: A new tool to predict the lithiation process of organic battery materials. *The Journal of Physical Chemistry Letters*, 9(13), 3573–3579. https://doi.org/10.1021/acs.jpclett.8b01123

[30] Gadre, S. R., Suresh, C. H. & Mohan, N. (2021). Electrostatic potential topology for probing molecular structure, bonding and reactivity. *Molecules*, 26(11), 3289. https://doi.org/10.3390/molecules26113289

[31] Badeji, A. (2025). Benzotrithiophene derivative as a corrosion inhibitor: Insights from density functional theory and Monte Carlo simulation studies. *Journal of Science and Information Technology*, 19(1), 10–22.

[32] Bradley, J. D. & Gerrans, G. C. (1973). Frontier molecular orbitals. A link between kinetics and bonding theory. *Journal of Chemical Education*, 50(7), 463. https://doi.org/10.1021/ed050p463

[33] Kateris, N., Xu, R. & Wang, H. (2023). HOMO-LUMO energy gaps of complexes of transition metals with single and multi-ring aromatics. *Combustion and Flame*, 257, 112513.

[34] Saidj, M., Djafri, A., Rahmani, R., Belkafouf, N. E. H., Boukabcha, N., Djafri, A. & Chouaih, A. (2023). Molecular structure, experimental and theoretical vibrational spectroscopy, (HOMO-LUMO, NBO) investigation, (RDG, AIM) analysis, (MEP, NLO) study and molecular docking of Ethyl-2-{[4-Ethyl-5-(Quinolin-8-yloxyMethyl)-4H-1,2,4-Triazol-3-yl] Sulfanyl} Acetate. *Polycyclic Aromatic Compounds*, 43(3), 2152–2176. https://doi.org/10.1080/10406638.2022.2039238

[35] Huang, Y., Rong, C., Zhang, R. & Liu, S. (2017). Evaluating frontier orbital energy and HOMO/LUMO gap with descriptors from density functional reactivity theory. *Journal of Molecular Modeling*, 23(1), 3. https://doi.org/10.1007/s00894-016-3175-x

[36] Dennington, R., Keith, T. & Millam, J. (2016). Gauss View, Version 6.0. 1.6, Semichem Inc., Shawnee Mission, KS, 2016.

[37] Andrienko, G. (2010). Chemcraft-graphical software for visualization of quantum chemistry computations. *See Https://Www. Chemcraftprog. Com*.

[38] Awas, E. O., Midiwo, J. O., Omosa, L. K., Derese, S., Kiganda, I., Omole, R. A., Akala, H. M., Ochora, D. O., Obakachi, V. A., Olalekan, S., Govender, K. K. & Nchiozem-Ngnitedem, V.-A. (2025). *In vitro*, ex vivo, and in silico studies of phytochemicals from the stem bark of Bischofia javanica. *Natural Product Research*, 1–7. https://doi.org/10.1080/14786419.2025.2521380

[39] Oladipo, S., Adeleke, A. A., Badeji, A. A., Babalola, K. I., Labulo, A. H., Hassan, I., Yussuf, S. T. & Olalekan, S. O. (2024). Computational investigation and biological activity of selected Schiff bases. *Journal of the Nigerian Society of Physical Sci.*, 2103–2103. https://doi.org/10.46481/jnsps.2024.2103

[40] Dileep, K. V., Ihara, K., Mishima-Tsumagari, C., Kukimoto-Niino, M., Yonemochi, M., Hanada, K., Shirouzu, M. & Zhang, K. Y. J. (2022). Crystal structure of human acetylcholinesterase in complex with tacrine: Implications for drug discovery. *Int. J. of Biol. Macromolecules*, 210, 172–181. https://doi.org/10.1016/j.ijbiomac.2022.05.009

[41] Viayna, E., Coquelle, N., Cieslikiewicz-Bouet, M., Cisternas, P., Oliva, C. A., Sánchez-López, E., Ettcheto, M., Bartolini, M., De Simone, A., Ricchini, M., Rendina, M., Pons, M., Firuzi, O., Pérez, B., Saso, L., Andrisano, V., Nachon, F., Brazzolotto, X., García, M. L., … Muñoz-Torrero, D. (2021). Discovery of a potent dual inhibitor of acetylcholinesterase and butyrylcholinesterase with antioxidant activity that alleviates Alzheimer-like pathology in old APP/PS1 mice. *Journal of Medicinal Chemistry*, *64*(1), 812–839. https://doi.org/10.1021/acs.jmedchem.0c01775

[42]. Scott, J. D., Li, S. W., Brunskill, A. P. J., Chen, X., Cox, K., Cumming, J. N., Forman, M., Gilbert, E. J., Hodgson, R. A., Hyde, L. A., Jiang, Q., Iserloh, U., Kazakevich, I., Kuvelkar, R., Mei, H., Meredith, J., Misiaszek, J., Orth, P., Rossiter, L. M., … Stamford, A. W. (2016). Discovery of the 3-Imino-1,2,4-thiadiazinane 1,1-Dioxide derivative verubecestat (MK-8931)–A β-Site amyloid precursor protein cleaving enzyme 1 inhibitor for the treatment of Alzheimer's disease. *J. of Medicinal Chemistry*, 59(23), 10435–10450. https://doi.org/10.1021/acs.jmedchem.6b00307

[43] Shelley, J. C., Cholleti, A., Frye, L. L., Greenwood, J. R., Timlin, M. R. & Uchimaya, M. (2007). Epik: A software program for pK a prediction and protonation state generation for drug-like molecules. *Journal of Computer-Aided Molecular Design*, 21(12), 681–691. https://doi.org/10.1007/s10822-007-9133-z

[44] Jacobson, M. P., Pincus, D. L., Rapp, C. S., Day, T. J. F., Honig, B., Shaw, D. E. & Friesner, R. A. (2004). A hierarchical approach to all-atom protein loop prediction. *Proteins: Structure, Function, and Bioinformatics*, 55(2), 351–367. https://doi.org/10.1002/prot.10613

[45] Friesner, R. A., Banks, J. L., Murphy, R. B., Halgren, T. A., Klicic, J. J., Mainz, D. T., Repasky, M. P., Knoll, E. H., Shelley, M., Perry, J. K., Shaw, D. E., Francis, P. & Shenkin, P. S. (2004). Glide: A new approach for rapid, accurate docking and scoring. 1. Method and Assessment of Docking Accuracy. *Journal of Medicinal Chemistry*, 47(7), 1739–1749. https://doi.org/10.1021/jm0306430

Citing this Article

Badeji, A. A., Samuel, O., Oladipo, S. D., Osinubi, A. D., Osanyinbi, A. A., & Akinbulu, I. A. (2026). Computational investigation of 2,3-dihydroquinazolin-4(1H)-one derivatives as multitarget anti-Alzheimer agents: DFT and molecular docking studies against AChE, BChE, and BACE1. *Lafia Journal of Scientific and Industrial Research, 4*(2), 42–59. https://doi.org/10.62050/ljsir2026.v4n2.876